International Journal of Plasticity 120 (2019) 361–379

Contents lists available at ScienceDirect

International Journal of Plasticity

journal homepage: www.elsevier.com/locate/ijplas

Material response, localization and failure of an aluminum alloy under combined shear and tension: Part II analysis

Kelin Chen, Martin Scales, Stelios Kyriakides*

Research Center for Mechanics of Solids, Structures & Materials, ASE, The University of Texas at Austin, Austin, TX 78712, USA

ARTICLE INFO

Keywords:
Combined shear and tension
Low triaxiality
Localization
Anisotropic plasticity
Material hardening

ABSTRACT

The responses of the tubular specimens loaded under combined tension and torsion in Part I exhibited limit load instabilities followed by extensive localized deformation prior to failure. The present manuscript outlines an analytical framework that aims to establish the extent to which plasticity can reproduce the measured responses up to the onset of failure without the introduction of damage-induced softening effects. The analysis incorporates a suitably calibrated non-quadratic anisotropic yield function, a material hardening response extracted to large strains from a simple shear test, and a finite element model with refined 3-D elements. The analysis successfully reproduces the shear and axial stress levels during the homogeneous deformation parts of the response, the stresses and deformations at the load maxima, and the parts with decreasing stress associated with localized deformation. Furthermore, the geometry of the necked zones and the rapid growth of strain inside them are reproduced to levels that correspond to the recorded failure strains. Critical aspects of this successful effort are the non-quadratic anisotropic yield function and the material hardening adopted. It is concluded that the framework developed, combined with a suitable failure criterion based on results like those in Part I, constitute a viable tool for establishing the end of life of structures in engineering practice.

1. Introduction

Part I describes in detail the conduct and the results of a set of tension-torsion experiments on custom Al-6061-T6 thin-walled tubes used to establish the failure strain in the moderate to low triaxiality regime. The specimen design and the stiff test setup enabled localization in the form of defuse necking to develop free of constrains until rapture occurred in the deepest part of the neck. High resolution DIC enabled continuous monitoring of the strain in the test section including the necked zone. The strains measured in the failure zone follow the classical trend of monotonic decrease with increasing triaxiality, but their values are significantly larger than previously reported ones. Both of these findings are in agreement with similar results in Scales et al. (2016). The failure surfaces were found to have the usual dimpled relief suggestive of ductile failure by void growth and coalescence. X-ray tomography and microscopic observations (e.g., Ghahremaninezhad and Ravi-Chandar (2012, 2013); Haltom et al. (2013)) found that this alloy had very small initial porosity and very limited pore growth away from the failure zone; it was further concluded that in the failure zone void growth and coalescence occurred very close to the end of life of the material.

Collectively these results prompt the present modeling effort that aims to establish the extent to which plasticity can reproduce the measured responses and the evolution of localization without the introduction of damage. To this end Part II presents: (a) the calibration of the anisotropic yield function of Barlat et al. (2005) Yld04-3D based on the tension-torsion and pressure-tension results

* Corresponding author.
E-mail address: skk@mail.utexas.edu (S. Kyriakides).

https://doi.org/10.1016/j.ijplas.2019.04.002
Received 12 January 2019; Received in revised form 14 March 2019; Accepted 4 April 2019
Available online 13 April 2019

in Part I. (b) The extraction of the material hardening response from a simple shear test using the calibrated Yld04-3D constitutive model as well as quadratic and non-quadratic isotropic yield functions. (c) The implementation of the constitutive models and the associated material hardening responses in an appropriately discretized finite element model of the tension-torsion test specimens; and (d) the use of this framework to simulate numerically the tension-torsion experiments. Particular emphasis is given to the effects of the constitutive model adopted and material hardening used on the calculated overall nominal stress-deformations responses, and on the onset and evolution of localization.

2. Constitutive behavior

2.1. Yield functions

It is now well established that the constitutive model used in the analysis of forming and other large deformation processes can influence the prediction of localization and failure in thin-walled structures. The use of more advanced non-quadratic yield functions that can account for prevailing anisotropies are thus preferred in modern studies and practices. Thus the main model adopted in this study is Barlat et al. (2005) Yld04-3D (e.g., see Korkolis and Kyriakides (2008, 2009), Korkolis et al. (2010) who used Yld 2000-2D; Giagmouris et al. (2010), Tian et al. (2017), Chen et al. (2016, 2018a), Dick and Yoon (2018), Lee et al. (2018), Ha et al. (2018) who used Yld04-3D, and Gorji and Mohr (2018) who used Yld 2000-3D). For comparison isotropic plasticity is modeled through Hosford's (1972) non-quadratic yield function, which in terms of the principal values of the stress deviator is given by:

$$\Phi = [(|s_1 - s_2|^k + |s_2 - s_3|^k + |s_3 - s_1|^k)/2]^{1/k}. \tag{1}$$

For completeness the von Mises quadratic yield function, i.e., $k = 2$ in (1), will also be used to simulate the tension-torsion experiments.

Barlat et al. (2005)introduce orthotropic anisotropy into (1) through two linear transformations to construct the tensors $\mathbf{S}'$ and $\mathbf{S}''$ from the Cauchy stress as follows:

$$\mathbf{S}' = \mathbf{C}'\mathbf{s} = \mathbf{C}'\mathbf{T}\boldsymbol{\sigma} = \mathbf{L}'\boldsymbol{\sigma} \text{ and } \mathbf{S}'' = \mathbf{C}''\mathbf{s} = \mathbf{C}''\mathbf{T}\boldsymbol{\sigma} = \mathbf{L}''\boldsymbol{\sigma} \tag{2a}$$

where $\mathbf{C}'$, $\mathbf{C}''$, $\mathbf{T}$, $\mathbf{L}'$, $\mathbf{L}''$ are transformation tensors. $\boldsymbol{T}$ transforms $\boldsymbol{\sigma}$ to $\mathbf{s}$ and $\mathbf{C}'$, $\mathbf{C}''$ contain the following anisotropy parameters.

$$\boldsymbol{C}' = \begin{bmatrix} 0 & -c'_{12} & -c'_{13} & 0 & 0 & 0 \\ -c'_{21} & 0 & -c'_{23} & 0 & 0 & 0 \\ -c'_{31} & -c'_{32} & 0 & 0 & 0 & 0 \\ 0 & 0 & 0 & c'_{44} & 0 & 0 \\ 0 & 0 & 0 & 0 & c'_{55} & 0 \\ 0 & 0 & 0 & 0 & 0 & c'_{66} \end{bmatrix}, \quad \boldsymbol{C}'' = \begin{bmatrix} 0 & -c''_{12} & -c''_{13} & 0 & 0 & 0 \\ -c''_{21} & 0 & -c''_{23} & 0 & 0 & 0 \\ -c''_{31} & -c''_{32} & 0 & 0 & 0 & 0 \\ 0 & 0 & 0 & c''_{44} & 0 & 0 \\ 0 & 0 & 0 & 0 & c''_{55} & 0 \\ 0 & 0 & 0 & 0 & 0 & c''_{66} \end{bmatrix}. \tag{2b}$$

The yield function in terms of the principal values of $\mathbf{S}'$ and $\mathbf{S}''$ is then expressed as:

$$\Phi = [(|S'_1 - S''_1|^k + |S'_1 - S''_2|^k + |S'_1 - S''_3|^k + |S'_2 - S''_1|^k + |S'_2 - S''_2|^k + |S'_2 - S''_3|^k + |S'_3 - S''_1|^k + |S'_3 - S''_2|^k + |S'_3 - S''_3|^k)/4]^{1/k} \tag{3}$$

where again k is assigned the value 8 (Logan and Hosford, 1980). Details about the derivations and the derivatives of the yield function with respect to the stress components can be found in Barlat et al. (2005) and Yoon et al. (2006) (the model is implemented in a subroutine developed by Yoon (2011)).

The model is calibrated using the responses of the 7 tension-torsion experiments, a “plane strain” tension test, a simple shear test, and a uniaxial tension test on an axial strip all extracted from the same batch of tubes. These were supplemented with results from the 7 tension-internal pressure radial path experiments. The state of stress and the strain ratios are evaluated for each experiment at a chosen value of plastic work (W^p= 1000 psi—6.897 MPa). Details of the calibration process followed are given in Appendix A. The anisotropy parameters determined from the process are listed in Table 1. (Note that the cylindrical coordinate system used is the one defined in Fig. 1, [I] and Fig. 2. It is different from the more conventional cylindrical coordinate system used for example in ABAQUS).

As noted by previous researchers, the results of such calibration processes are not unique. To further evaluate the present solution the calibrated yield function and some of the corresponding experimental points are compared in Fig. 1a (T-T ≡ Tension-Torsion, P-T ≡ Pressure-Tension). Plotted are the work contours in the hoop-axial stress plane, $\sigma_{11} - \sigma_{22}$, both normalized by the measured axial stress σ^w_{22} at W^p= 1000 psi (6.897 MPa) for different values of normalized shear stress σ_{12}. The comparison of experimental data and the calibrated work contours is deemed as satisfactory. A work contour in the $\sigma_{22} - \sigma_{12}$ space, important to the problem at hand, is compared to measured tension-torsion data in Fig. 1b. The comparison is again favorable providing additional support for the soundness of the anisotropy calibration procedure. As mentioned in Section 3.1,[I] in the tension-torsion experiments the test section develops a small amount of non-uniform radial deformation in the form of bowing, which affects the hoop stress to some degree (σ_{11}). The hoop stress is assumed to be uniform and proportional to the axial stress, $\sigma_{11} = \beta\sigma_{22}$. The constant of proportionality varies with the radial path ratio α, and is determined as outlined in Appendix B.

[I] refers to Sections, Figures and Equations of Part I.

Table 1
Anisotropy parameters for Yld04-3D model.

c'_{12}	c'_{13}	c'_{21}	c'_{23}	c'_{31}	c'_{32}	c'_{44}	c'_{55}	c'_{66}
1.028	1.150	1.162	0.941	0.679	0.985	1.0	1.0	1.367
c''_{12}	c''_{13}	c''_{21}	c''_{23}	c''_{31}	c''_{32}	c''_{44}	c''_{55}	c''_{66}
0.713	0.683	0.847	1.093	1.056	0.962	1.0	1.0	0.695

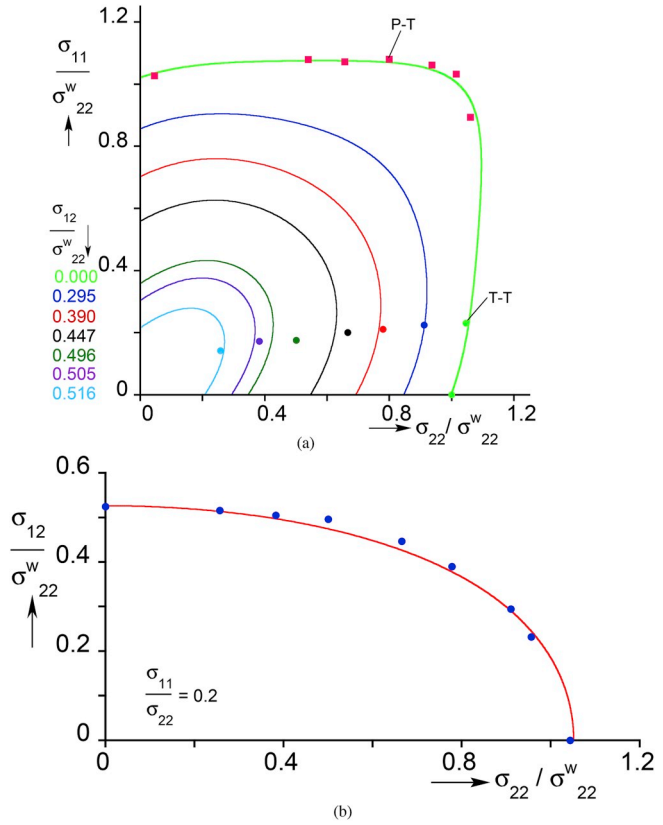

Fig. 1. (a) Work contours of the calibrated Yld04-3D constitutive model in the axial and hoop stress space at varying levels of shear. Experimental data used in calibration are included with solid bullets (T-T≡ tension-torsion, P-T≡ pressure-tension). (b) Work contour in the shear-axial stress space for $\sigma_{11}/\sigma_{22} = 0.2$.

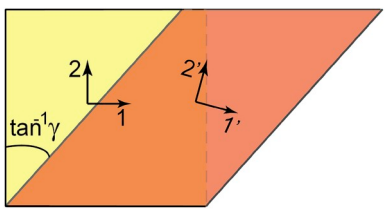

Fig. 2. Material element under simple shear; shown are the initial and rotated material axes.

2.2. Material hardening

The material response is commonly measured in a uniaxial tension test, which usually necks at a strain of a few percent. By contrast, simple shear tests remain free of instabilities to large strains and thus offer an attractive alternative. Since the present study involved tension-torsion of tubes, it was convenient to extract the material hardening from a pure torsion experiment on a tube that originated from the same batch as those of the biaxial specimens. Since the response is influenced by the constitutive model adopted

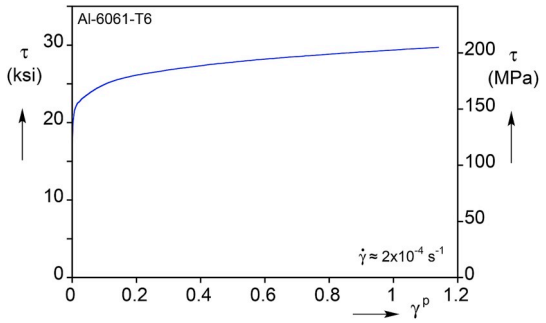

Fig. 3. Measured shear stress-plastic shear strain ($\tau - \gamma^p$) response for the Al-6061-T6 tube analyzed.

(e.g., see Tardif and Kyriakides, 2012; Chen et al., 2018a; Kang et al., 2008), it is extracted for each of the three constitutive models considered. Furthermore, Chen et al. (2018b) showed that in the case of simple shear tests, the material axes rotate during shearing, and this must be accounted for when the material exhibits plastic anisotropy (see also Ch. XII-1 in Hill, 1950; ABAQUS, 2016). This section discusses the extraction process.

The specimen overall geometry is the same as in Fig. 1,[I] but the test section wall thickness was increased to 0.0461 in (1.17 mm) in order to delay buckling. The specimen was twisted under rotation control producing a shear strain rate of approximately 2×10^{-4} s^{-1}, while the axial load was prescribed to remain at zero.

The shear stress, τ, is calculated directly from the recorded torque using the thin-walled geometry of the test section. The deformation in the test section was monitored using DIC (see Section 2.3,[I]) with the deformation gradient, $\boldsymbol{F}$, being provided directly from the ARAMIS software. The deformation in the test section was found to remain quite uniform, but $\boldsymbol{F}$ was averaged over a zone 0.2×0.4 in (5.1×10.2 mm) in the center of the test section. For the case of simple shear, $\boldsymbol{F}$ is given by

$$\boldsymbol{F} = \begin{bmatrix} 1 & \gamma & 0 \\ 0 & 1 & 0 \\ 0 & 0 & 1 \end{bmatrix}, \tag{4}$$

where γ is defined in Fig. 2. The incremental strain tensor is then given by

$$d\varepsilon = sym(d\boldsymbol{F}\boldsymbol{F}^{-1}) = \begin{bmatrix} 0 & d\gamma/2 & 0 \\ d\gamma/2 & 0 & 0 \\ 0 & 0 & 0 \end{bmatrix}. \tag{5}$$

Fig. 3 shows the shear stress-plastic shear strain ($\tau - \gamma^p$) response measured in this experiment. It extends to a strain of just under 1.2 and exhibits hardening throughout.

The incremental spin tensor is given by

$$d\omega = skewsym(d\boldsymbol{F}\boldsymbol{F}^{-1}) = \begin{bmatrix} 0 & d\gamma/2 & 0 \\ -d\gamma/2 & 0 & 0 \\ 0 & 0 & 0 \end{bmatrix}, \tag{6a}$$

$$\text{which integrates to } \omega = \begin{bmatrix} 0 & \gamma/2 & 0 \\ -\gamma/2 & 0 & 0 \\ 0 & 0 & 0 \end{bmatrix} \tag{6b}$$

Thus, the transformation tensor for the material frame becomes

$$\boldsymbol{A} = \begin{bmatrix} \cos\gamma/2 & -\sin\gamma/2 & 0 \\ \sin\gamma/2 & \cos\gamma/2 & 0 \\ 0 & 0 & 1 \end{bmatrix}. \tag{7}$$

The stress, when rotated into the material frame, is then:

$$\boldsymbol{\sigma}' = \boldsymbol{A}\sigma\boldsymbol{A}^T = \tau \begin{bmatrix} -\sin\gamma & \cos\gamma & 0 \\ \cos\gamma & \sin\gamma & 0 \\ 0 & 0 & 1 \end{bmatrix}. \tag{8}$$

For the anisotropic material in Eqs. (2) and (3), the equivalent stress in the material frame then becomes

$$\sigma_e = \sigma_e(\sigma'_{ij}, c'_{ij}, c''_{ij}). \tag{9a}$$

By contrast, in the reference frame it is given by

$$\sigma_e = \sigma_e(\sigma_{ij}, c'_{ij}, c''_{ij}). \tag{9b}$$

The equivalent stress is then used to evaluate the work compatible plastic equivalent strain increment at stage n in the incremental process from

$$d\varepsilon_e^p|_n = \left.\frac{\tau d\gamma^p}{\sigma_e}\right|_n . \tag{10}$$

The complete response is assembled by summing the increments over the whole test history (see Eq. (12),[I]). If the material yields isotropically, (3) reduces to the Hosford's non-quadratic yield function (1) with exponent 8 (H8). This is invariant to transformation and, as a result, the simple shear test reduces to:

$$\sigma_e|_{\mathrm{H8}} = (2^7 + 1)^{1/8}\,\tau \tag{11a}$$

and

$$d\varepsilon_e^p|_{\mathrm{H8}} = \frac{d\gamma^p}{(2^7 + 1)^{1/8}}, \tag{11b}$$

which integrates directly.

To facilitate a comparison with a quadratic yield function, we include the equivalent stress for simple shear for von Mises (vM)

$$\sigma_e|_{\mathrm{vM}} = \sqrt{3}\,\tau. \tag{12a}$$

The corresponding equivalent plastic strain increment is

$$d\varepsilon_e^p|_{\mathrm{vM}} = \frac{d\gamma^p}{\sqrt{3}}, \tag{12b}$$

which also integrates directly.

The anisotropy parameters in Table 1 and the measured shear stress and strain values were used in Eqs. (9a) and (10) to generate incrementally the equivalent stress-equivalent plastic strain response of the material. It is referred to as the *Material Frame* (MF) response and is plotted in Fig. 4a. Included is the corresponding response when the rotation of the material frame is not accounted for—referred to as *Reference Frame* response (RF). Clearly, this particular anisotropy leads to progressive reduction in tangent modulus for equivalent strains larger than about 0.1. In Section 3.2 it will be demonstrated that such changes in modulus can have a significant influence on the prediction of localization and other instabilities and the onset of failure (Chen et al. (2018b) examine how the material frame rotation affects the extraction of the hardening response for the Hill-48 anisotropic yield function.).

Fig. 4b shows the equivalent stress-equivalent plastic strain responses corresponding to the isotropic von Mises and Hosford yield functions. Included is the Reference Frame response based on the Yld04-3D anisotropic yield function. The three responses exhibit

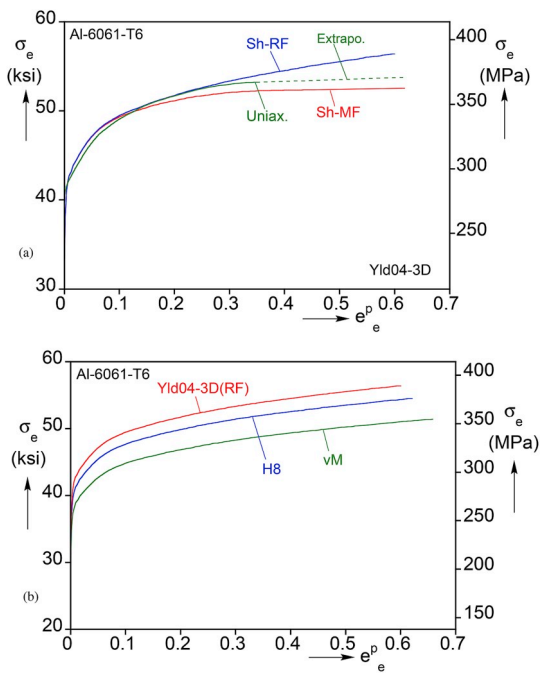

Fig. 4. (a) The *Material* and *Reference Frame* equivalent stress-equivalent plastic strain responses extracted from the measured $\tau - \gamma^p$ response. Included is the material response from a uniaxial tension test–"Uniax." (b) Comparison of the Reference Frame equivalent stress-equivalent plastic strain response with the isotropic von Mises and Hosford responses.

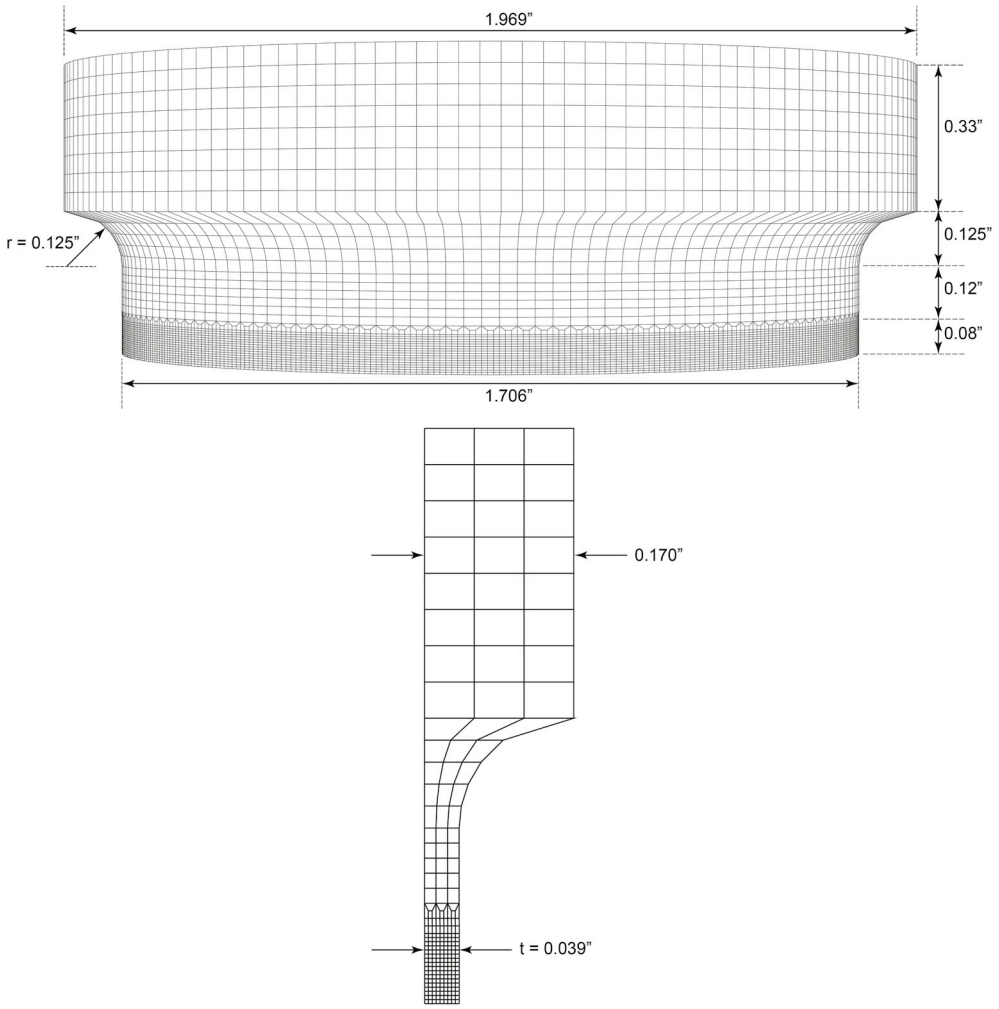

Fig. 5. Tension-torsion tubular specimen finite element mesh used to simulate the experiments.

similar hardening, but trace different stress levels. The difference in stress level between H8 and Yld04-3D is caused by the anisotropy, whereas the difference between vM and H8 is due to the different exponent of the two yield functions.

In order to facilitate a comparison with the response in Fig. 4, the material hardening was also measured in an independent uniaxial tension test. The test was performed on an axial specimen machined out of tube No. 3. The nominal stress achieved a maximum at a strain of only 7%; thus the response was extrapolated using the inverse method of Tardif and Kyriakides (2012). The location of the neck was controlled by machining a large radius into the sides of the test specimen, and the deformation in this zone was monitored with DIC. Several constitutive models were used in the extrapolation. The response identified as “Uniax.” in Fig. 4a was evaluated using the Yld04-3D constitutive model as calibrated in Section 2.1 and Appendix A. The data extend to a strain of about 35% when the specimen failed in the neck. To accommodate the needs of the present study, the response was linearly extrapolated to the same strain level as that of the simple shear test (extrapolation based on the slope of the last 2 points). The uniaxial response traces a slightly lower stress up to a strain of about 0.12 and overshoots the shear response at higher strains.

3. Numerical simulation of the tension-torsion experiments

3.1. Finite element model

A finite element model of the tubular test specimens and setup shown in Fig. 1,[I] developed in ABAQUS is now used in conjunction with the constitutive models outlined in Section 2 to simulate the tension-torsion experiments individually. Symmetry about the center of the test section is assumed, which allows consideration of only half of the tubular test specimen as illustrated in Fig. 5. It consists of a 0.330 in (8.38 mm) long thicker upper section, a 0.200 in (5.08 mm) straight test section, connected with a 0.125 in (3.18 mm) radius fillet. The specimen has an axially uniform inner surface with a radius of 0.815 in (20.5 mm); the thicker section has a wall thickness of 0.170 in (4.32 mm) and the test section is assigned the average wall thickness of the specific test specimen analyzed (typically t_o= 0.039 in–1.0 mm).

The model is meshed with solid elements (C3D8R) as follows:

- A 0.08 in (2.0 mm) long part of the test section adjacent to the symmetry plane has 9 elements through the thickness and 450 elements around the circumference in order to facilitate the development of the expected localization.
- The rest of the straight test section has a courser mesh with 3 elements through the thickness and 150 around the circumference.
- The thick upper section has the same mesh distribution and consequently larger elements.
- The fillet also has the same mesh distribution as the two sections it joins so the element size along the length is adjusted to comply with the curvature of the fillet.

The measured wall eccentricity of each specimen, listed in Table 1,[I] is incorporated into the model by shifting the inner cylindrical surface relative to the outer one by the required amount, which changes slightly the mesh dimensions.

The degrees of freedom of nodes on the symmetry plane are constrained except that they are free to move in the radial direction. The complex clamping of the specimen used in the experiments was not reproduced in the model. Instead, a reference node was created which is kinematically coupled to the nodes of the upper surface. The specimen was loaded as follows:

- For $\alpha < 3$ the angle of rotation of the reference node is prescribed incrementally causing a change in the torque, which is monitored by a "sensor." An axial force increment is then prescribed through a user subroutine (UAMP) to generate the required axial force-torque proportionality (similar schemes used in Papasidero et al., 2014; Xue et al., 2013).
- For $\alpha \geq 3$ the axial displacement of the reference node is prescribed incrementally resulting in a force registered by the sensor. A torque increment is then prescribed through the UAMP to generate the required axial force-torque proportionality.

3.2. Simulation of the $\alpha = 0.75$ tension-torsion radial path experiment

The results of the simulation of the experiment with $\alpha = 0.75$ are now used to illustrate the performance of the numerical modeling effort. The experiment was simulated using the vM, H8 and Yld04-3D constitutive models, along with the corresponding material stress-strain response of each (Figs. 3 and 4). Fig. 6 compares the three calculated nominal shear stress-rotation and axial stress-elongation responses to the experimental ones. As in the experiments, the rotation and elongation are evaluated from the edges of the test section. The three simulations match the experimental responses closely up to yielding. Subsequently, the numerical responses trace mildly hardening trajectories that mimic the experimental one, and develop a limit load followed by a decaying branch, an indication that deformation is localizing (△ ≡ limit load). The limit load is the result of tension-induced wall thinning which is also responsible for the subsequent downturn in the nominal stress responses. It is worth remembering that by contrast, under pure torsion the test section wall thickness section does not change and deformation does not localize (see Section 3.2,[I]). The

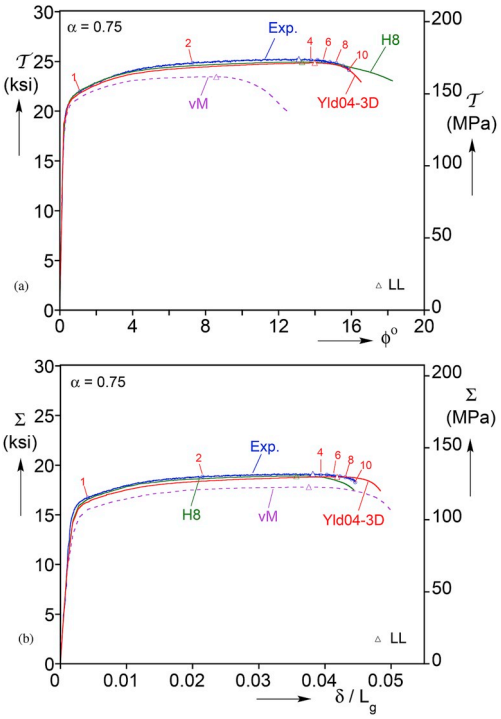

Fig. 6. Comparison of measured and predicted responses using three different constitutive models for $\alpha = 0.75$. (a) Shear stress-rotation and (b) axial stress-elongation. The symbols "△" correspond to the nominal stress maxima or "limit loads."

H8 and Yld04-3D responses match the experimental one very well up to the limit load whereas vM underestimates both the axial and shear stress experimental values. Furthermore, the shear maximum of vM occurs at a much smaller rotation.

Because the limit loads correspond to the onset of localization, a critical stress state in manufacturing, it is useful to compare the limit states obtained using the classical analytical Considère condition with the FE model values. If elastic deformations and the small radial deflection of the test section are neglected, this condition reduces to:

$$\left.\frac{d\sigma_{22}}{d\varepsilon_{22}}\right|_c = \sigma_{22c}. \tag{13a}$$

(2- is the axial direction). It can be shown that for isotropic yield functions this implies that

$$\left.\frac{d\sigma_e}{d\varepsilon_e^p}\right|_c = \sigma_e \left.\frac{\partial \Phi}{\partial \sigma_{22}}\right|_c, \tag{13b}$$

where Φ is the yield function, σ_e is the associated equivalent stress, and $d\varepsilon_e^p$ the work compatible equivalent plastic strain increment. For vM (13b) becomes

$$\left.\frac{d\sigma_e}{d\varepsilon_e}\right|_c = \frac{\sqrt{3}\,\sigma_{ec}}{2[1+4/\alpha^2]^{1/2}}. \tag{14}$$

The equivalent strain at the limit load can be evaluated from (14) using the material response for vM extracted from the simple shear test in Fig. 4b. For $\alpha = 0.75$, $\varepsilon_{ec}^p = 0.247$, which compares with 0.244 from the FE model (taken from the mid-thickness at the symmetry plane). Similar level of agreement was found for all radial paths with $\alpha \geq 0.5$. For even smaller values of α, localization becomes increasingly more difficult to achieve numerically requiring the introduction of a small thickness imperfection in the FE model.

The critical state for H8 can be similarly derived analytically from (13 b) while Yld04-3D requires numerical treatment. Overall, the critical strain predicted for all three constitutive models was found to be within a few percent of the values from the full finite element simulations. This points to the usefulness of the Considère type analysis for estimating the limit states for uniform axial-shear stress states.

We now compare additional aspects of the numerical simulations to the experimental results in some detail. Fig. 7a compares the radial deflection across the test section predicted using Yld04-3D with the measured values at the three stations marked on the experimental responses in Fig. 5,[I] — profiles ③ correspond to the location of the limit load in the experiment. The predicted profiles are in good agreement with the measured values. This agreement is another indication of the success of the Yld04-3D calibration scheme used. It is worth pointing out that although for smaller values of α the radial deformation is quite small, the stress inhomogeneity caused by it is sufficient to trigger localization without the need for a geometric imperfection perturbation for all values of biaxiality ratios considered except for $\alpha = 0.5$. For the smallest α the induced radial deformation is too small, so localization was

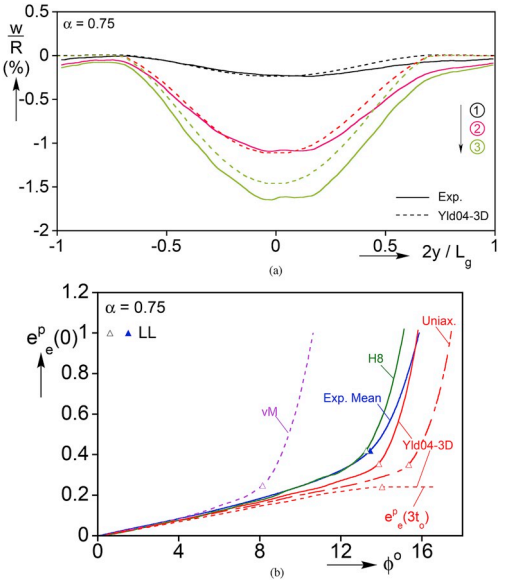

Fig. 7. (a) Comparison of measured and calculated radial displacement profiles across the length of the test section for $\alpha = 0.75$, for the first three stations marked in Fig. 6. (b) Measured *Mean* equivalent plastic strain in the localizing zone vs. rotation for $\alpha = 0.75$, and corresponding ones calculated using the vM, H8 and Yld04-3D constitutive models. Included is the strain at $3t_o$ above the localizing zone. Shown also is the response produced using the stress-strain response from the uniaxial test (see Fig. 4a). The symbols "△" correspond to the nominal stress maxima or "limit loads."

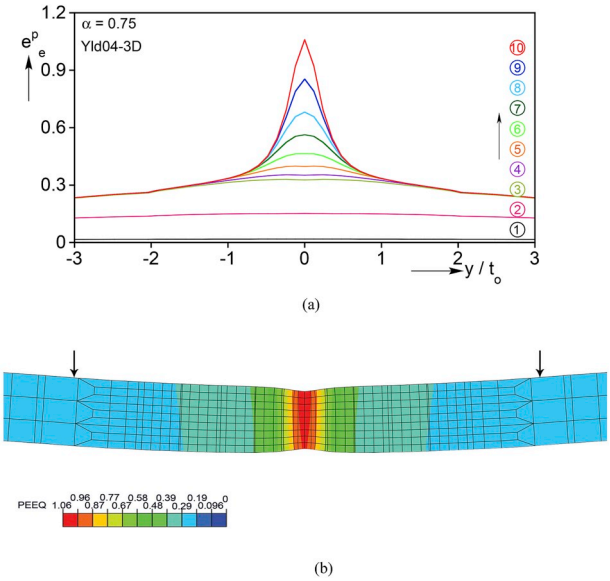

Fig. 8. (a) Calculated equivalent plastic strain profiles across the test section for $\alpha = 0.75$, at rotations corresponding to those on the numbered stations in Fig. 6. (b) Through-thickness view of the plane of symmetry (mirrored) showing the necked region corresponding station ⑩ in Figs. 6 and 8a—arrows are $6t_o$ apart.

induced by decreasing the wall thickness by 0.1% in a circular band $2t_o$ wide spanning the symmetry plane.

Beyond the limit loads, deformation localizes for all three constitutive models and both the nominal shear and axial stresses in Fig. 6 start to decrease. The decaying part of the vM shear response occurs early and the downturn is more pronounced. The Yld04-3D matches the experimental downturn very well and the H8 downturn occurs at a slower rotation rate. A diffuse neck approximately $2t_o$ wide starts to develop forming a circular band spanning the symmetry plane. Fig. 7b plots the equivalent plastic strain on the outer surface at the symmetry plane against the rotation angle from the three models (note that the variation in strain across the wall thickness is quite small). Included for comparison is the corresponding experimental plot. The three calculated trajectories track the experimental one up to their respective limit loads, and take a significant upturn thereafter. The H8 and Yld04-3D results follow the nearly exponential growth of the experimental trajectory very well. The vM trajectory on the other hand, although exhibiting a similar increasing trend, it takes place at a much smaller rotation because of the early development of the load maxima. The trajectories clearly indicate the significant shearing and axial deformation experienced in the localizing zone.

The evolution of the deformation in the localizing zone produced by the Yld04-3D model, is illustrated in Fig. 8a, which plots ten profiles of equivalent plastic strain over a $6t_o$ height across the band corresponding to the stations marked on the experimental responses with "○" symbols. Profiles ① and ② correspond to the early parts of the stress history so they show the deformation to be essentially uniform across this zone. Profile ③, which corresponds to the ϕ at the experimental load maxima, is also uniform but slightly bent upwards due to the radial deformation of the test section in Fig. 7a (note that the predicted load maximum occurs at a somewhat larger ϕ than in the experiment). Beyond this point deformation concentrates in a zone about $2t_o$ wide while outside the band the deformation remains relatively unchanged. This divergence in the deformation between points within and outside the localizing band is also illustrated in Fig. 7b, which includes the strain-rotation response outside the localizing zone at $x_2 = 3t_o$.

The neck that forms is seen to sharpen with the deformation concentrating in the central few elements. By station ⑩ the strain in the center of the neck has reached a value of about 1.0, which corresponds to the mean strain at failure reported in the experiment. Fig. 8b shows a cross sectional view of the necked zone at the plane of symmetry of the FE model at station ⑩. Superimposed are color contours corresponding to equivalent plastic strain. The upper edge represents the outer side of the specimen and the arrows indicate the $6t_o$ length captured in Fig. 8a. It is noteworthy that the localization is in the form of a diffuse neck as seen in experiments by sectioning. Furthermore, the deformation across the wall thickness is seen to be quite uniform (less than 1% difference between the center and the outer surface). The small curvature of the section is due to the radial deflection mentioned earlier. This zone was meshed with 9 nearly cubical elements across the wall thickness (see Fig. 5). This discretization roughly corresponds to that of the DIC, governed by the facet size and spacing, used to capture the deformation in the experiment (see Section 2.3,[l]). Increasing the number of elements in this zone does not change the width of the neck but allows sharper strain gradients to develop leading to an increase in the peak strain. Furthermore, in the absence of a failure criterion, the FE analysis must be terminated by the operator. Thus in Fig. 7b each of the three strain trajectories were terminated at a value of about 1.0, which is the mean measure of failure strain in the experiment.

For comparison purposes the $\alpha = 0.75$ experiment was also simulated using the material hardening response extracted from the uniaxial tension test for the same constitutive model–shown extrapolated in Fig. 4a. The shear-rotation and axial stress-elongation responses are compared to the ones based on the simple shear stress-strain response in Fig. 9. The two material models produce

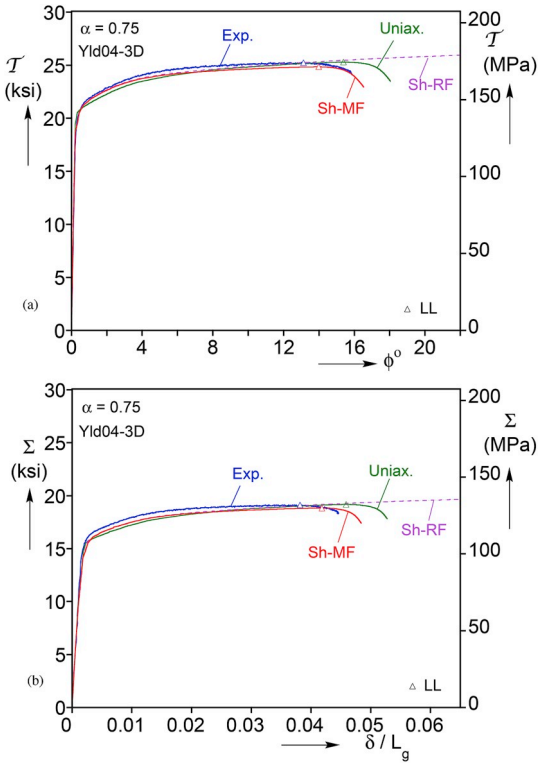

Fig. 9. Measured and predicted responses using the shear and uniaxial stress-strain responses for $\alpha = 0.75$. (a) Shear stress-rotation and (b) axial stress-elongation.

similar responses but the limit loads of the Uniax. material are delayed somewhat, while subsequently the stress drops at a similar rate. The effect of this difference on the equivalent strain at the symmetry plane, is illustrated in Fig. 7b. The trajectory of "Uniax." is similar to that from the Sh-MF model, but the upturn is now delayed moving from $\phi \approx 13.9°$ to $15.4°$. It must, however, be emphasized that the neighborhoods of the limit loads and beyond occur at high enough strains to be influenced by the extrapolation of the uniaxial response adopted. For completeness Fig. 9 includes responses based on the Reference Frame (RF) hardening curve (Fig. 4a) which, in the strain regime of interest here, is much stiffer than the Material Frame (MF) response. Consequently, the localization is delayed to strain levels much higher than those of the experiment.

3.3. Simulation of the $\alpha = 2.0$ tension-torsion radial path experiment

We now examine in some detail the results of the numerical simulations for $\alpha = 2.0$, which is representative of the more axial stress dominant stress paths considered. Figs. 10–13 present similar sets of results as those presented for $\alpha = 0.75$. Fig. 10 compare the shear-rotation and axial stress-elongation responses calculated using the three constitutive models with the experimental ones. The shear response is predicted very well by Yld04-3D including the limit load and the decaying part after it. H8 is very good up to the limit load, which however occurs slightly earlier causing the post-limit load response to start its downward trajectory somewhat earlier. The vM underpredicts the complete response for this case also. The axial stress responses for Yld04-3D and H8 follow each other closely. Their limit loads occur somewhat earlier and the decaying trajectories occur somewhat earlier than in the experimental response. The vM response underpredicts the complete experimental one again.

Fig. 11a compares the radial deflection across the test section predicted by the Yld04-3D analysis for three stations, with station ③ corresponding to the limit load in the experiment. The predicted deflections follow those measured very well. Higher axial stress is of course expected to result in deeper necking. However, the maximum value of the radial displacement at ③ is smaller than that in Fig. 7a, because here the limit load occurs at smaller overall strains.

Fig. 11b draws the evolution of strain with ϕ on the outer surface at the symmetry plane together with the corresponding experimental result. The Yld04-3D trajectory matches the experimental one very well in all respects. The H8 trajectory starts on the upward path earlier than the experiment, this despite producing stress responses that are close to those of Yld04-3D in Fig. 10. The vM trajectory is between those of Yld04-3D and H8. The results demonstrate that accurate prediction of the structural responses is not sufficient for evaluating the performance of each constitutive model.

Fig. 12a shows the evolution of deformation in the localization zone produced by Yld04-3D. Plotted are ten profiles of equivalent plastic strain that correspond to the stations marked on the measured stress-deformation responses in Fig. 10 with open symbols – ∧. Following the load maxima deformation localizes becoming progressively more concentrated in a zone about $3t_o$ tall while outside

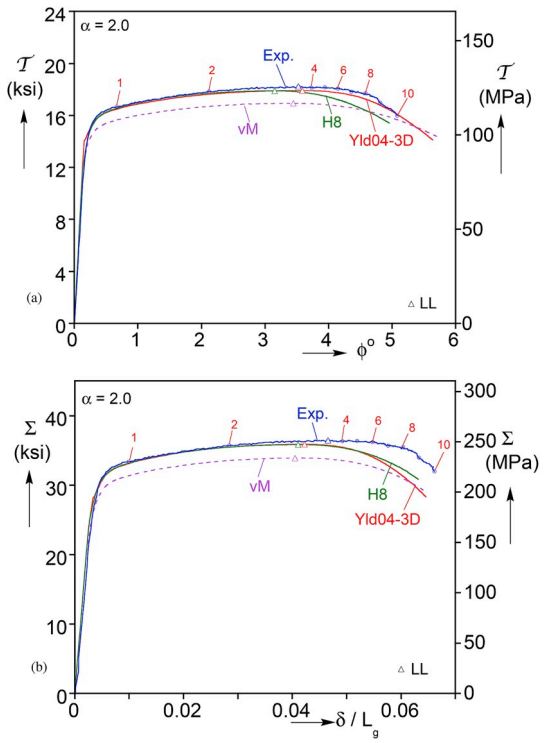

Fig. 10. Comparison of measured and predicted responses using three different constitutive models for $\alpha = 2.0$. (a) Shear stress-rotation and (b) axial stress-elongation.

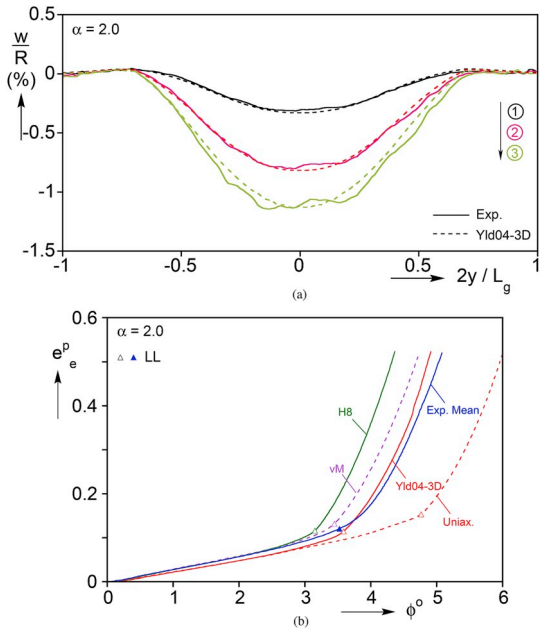

Fig. 11. (a) Comparison of measured and calculated radial displacement profiles across the length of the test section for $\alpha = 2.0$, for the first three stations marked in Fig. 10. (b) Measured *Mean* equivalent plastic strain in the localizing zone vs. rotation for $\alpha = 2.0$, and corresponding ones calculated using three different constitutive models. Included is the equivalent plastic strain predicted using the uniaxial stress-strain response.

this zone deformation remains essentially unchanged. In configuration ⑩, which corresponds to the last station before rupture occurred in the experiment, the strain in the neck is just under 0.6. This is significantly lower than the 1.0 strain achieved for $\alpha = 0.75$ at the point of rupture. A cross section of the necked region in this configuration is shown in Fig. 12b. Despite the smaller maximum strain, the neck is deeper and more defuse. Furthermore, the strain varies more across the wall thickness than for $\alpha = 0.75$ with the

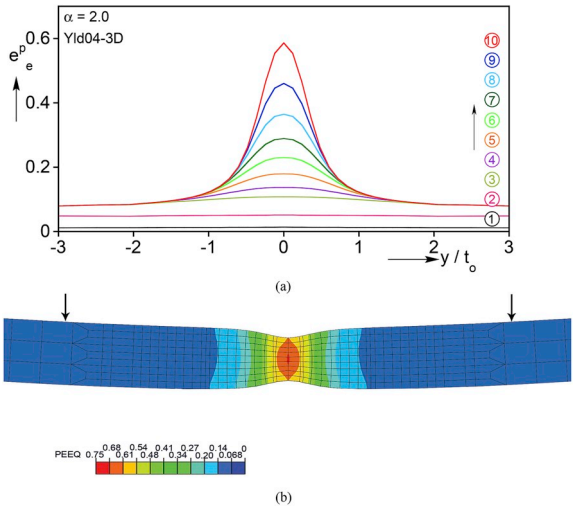

Fig. 12. (a) Calculated equivalent plastic strain profiles across the test section for $\alpha = 2.0$, at rotations corresponding to those on the numbered stations in Fig. 10. (b) Through-thickness view of the plane of symmetry (mirrored) showing the necked region corresponding station ⑩ in Figs. 10 and 12a—arrows are $6t_o$ apart.

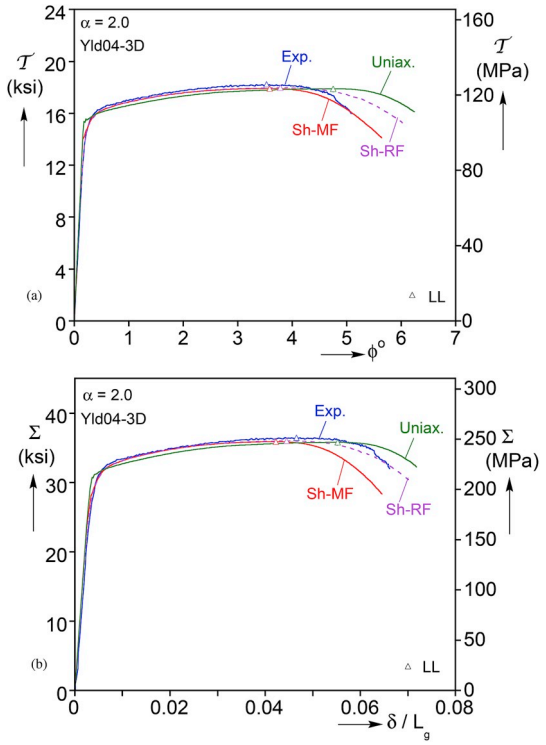

Fig. 13. Measured and predicted responses using the shear and uniaxial stress-strain responses for $\alpha = 2.0$. (a) Shear stress-rotation and (b) axial stress-elongation.

maximum being in the center where the strain is about 20% higher than on the outer surface. It's worth pointing out that in this configuration, the row of elements at the symmetry plane are rather elongated, which may affect the accuracy of the local strain. Further refinement of the mesh can improve the accuracy of the local strain when they are implemented in a failure criterion. Such a refinement has small influence on the calculated responses in Fig. 10.

Fig. 13 compares the shear stress-rotation and axial stress elongation responses produced using the simple shear (Sh-MF) and uniaxial (Uniax.) stress-strain responses, both based on Yld04-3D. The limit load of the $\mathscr{T} - \phi$ response based on the Uniax. Material is delayed compared to the experimental one and so is the decaying part. The same is the case for the $\Sigma - \delta$ response. This limit load occurs at a relative small strain ($\sim$0.12) where the Uniax. has a higher tangent modulus than the Sh-MF stress-strain response,

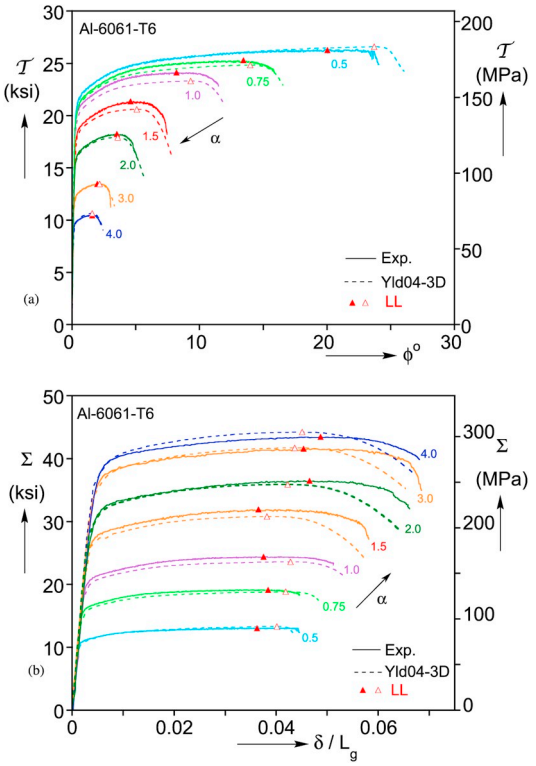

Fig. 14. Measured and predicted responses using the Yld04-3D constitutive model for the full set of radial path tension-torsion experiments performed. (a) Shear stress-rotation and (b) axial stress-elongation.

causing the observed difference in the limit load. The delay in the downturns of the two responses results in a significant delay in the rotation angle at which the upturn in the equivalent strain takes place in Fig. 11b.

3.4. Summary of simulation of all tension-torsion radial path experiments

All seven radial path tension-torsion experiments were simulated numerically and the same sets of results as those presented for $\alpha = 0.75$ and 2.0 were generated. For brevity here we present the predictions using Yld04-3D and limit discussion about the other two sets of predictions to general trends. Fig. 14 compares the calculated shear-rotation and axial stress-elongation responses using Yld04-3D with the experimental responses. The shear responses are uniformly in very good agreement with the measurements. The responses track the experimental ones very closely. The rotations at the limit loads are also in good agreement with those of the measured responses, except for $\alpha = 0.5$ where the predicted limit load is somewhat delayed. The decaying shear stress trajectories are also in very good agreement with the experimental ones. The corresponding H8 predictions follow the responses up to the limit loads. The limit loads tend to be somewhat delayed for low values of α causing a delay in localization, while for the axial stress dominant paths the responses are close to those of Yld04-3D. By contrast, the vM responses uniformly underpredict the experimental ones, and in most cases the limit load and the subsequent downturns are also missed.

The axial stress-elongation predicted using Yld04-3D track the experimental ones well up to the limit loads with the elongations at the limit load predicted adequately also. The localization parts of the responses that follow the stress maxima agree with the experimental ones for the three lower values of α, but undershoot them for the four higher stress ratios. The H8 responses follow the Yld04-3D ones closely and produce limit loads that are also close except for lower values of α. The post-limit load responses are close to those of Yld04-3D for higher stress ratios, but tend to localize early for the lower ones. The vM responses are also lower than the measured ones, the limit loads are mostly off, and the localizing sections occur either early or late.

Fig. 15 plots the equivalent plastic strain at the symmetry plane vs. rotation from the Yld04-3D predictions together with the corresponding results from the seven experiments. The predictions track the measured trajectories very well for the higher stress ratios. For the two lower values of α the trajectories undershoot the experimental ones up to the limit load but follow the experimental trend during the localization upturn. The ends of the experimental trajectories correspond to rupture, so the predictions were terminated at the same strain. It is noteworthy that the evolution of necking was captured with the same degree of success as in the two examples shown in Figs. 8b and 12b. Interestingly, the upturn of the strain-rotation for the H8 predictions occurs at a smaller value of ϕ than in the experimental results, much like the $\alpha = 2.0$ case in Fig. 11b. The predicted trajectory for the 0.5 stress ratio is an exception as here the upturn occurs well after the experimental one. The corresponding vM results are uniformly poor, particularly so for lower values of α. In summary, from these results we can conclude that use of a suitably calibrated non-quadratic yield function,

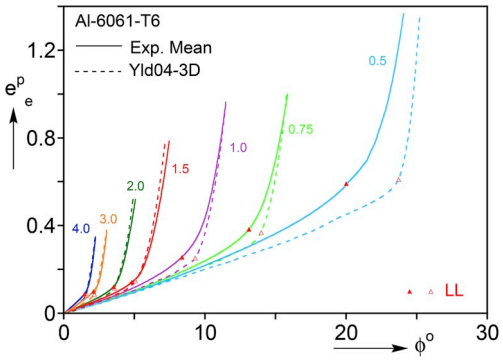

Fig. 15. Comparison of measured *Mean* equivalent plastic strain vs. rotation for full set of radial path experiments, and corresponding one calculated using Yld04-3D constitutive model.

together with a suitably extracted and calibrated material hardening response are essential for reproducing the response and localization that precedes failure. The introduction of anisotropy through the Yld04-3D model generally improves the predicted results particularly so for the evolution of localization.

3.5. Simulation of the corner path experiments

The $\alpha = 1.0$ and 2.0 families of corner paths reported in Part I were also simulated numerically and the predictions based on the Yld04-3D constitutive model is illustrated in Figs. 16–18. Fig. 16 compare the calculated and measured shear-rotation and axial stress-elongation responses for the radial, $\Sigma \rightarrow \mathscr{T}$ and $\mathscr{T} \rightarrow \Sigma$ paths for $\alpha = 1.0$. As reported earlier, the two calculated responses for the radial path reproduce the experimental trajectories but at somewhat lower stress levels. The predictions for the $\Sigma \rightarrow \mathscr{T}$ compare very well with the experimental responses. For the $\mathscr{T} \rightarrow \Sigma$ path the shear response is reproduced well but the axial response is underpredicted rather significantly. This may be related to the fact that the work contour of the calibrated Yld04-3D model corresponding to $\sigma_{12} = 0.496\sigma^w_{22}$ (i.e., $\alpha = 1.0$) undepredicted the experimental data point (see Fig. 1a) and this results in earlier yielding for this value of α. The equivalent strain-rotation results are compared to the measurements in Fig. 17a. Here the radial path trajectory is reasonably close to the measured one; the upswing of the $\Sigma \rightarrow \mathscr{T}$ response occurs somewhat earlier than the experiment, while the trajectory for the $\mathscr{T} \rightarrow \Sigma$ path is delayed compared to the experimental one.

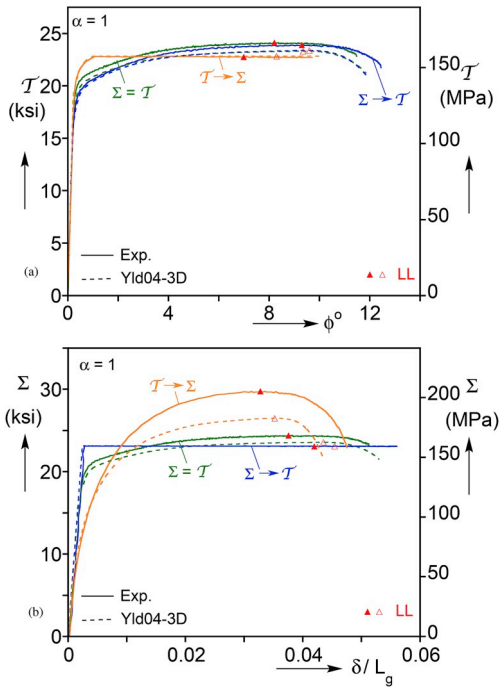

Fig. 16. Comparison of measured and calculated responses using Yld04-3D for the set of radial and corner path experiments with $\alpha = 1.0$. (a) Shear stress-rotation and (b) axial stress-elongation.

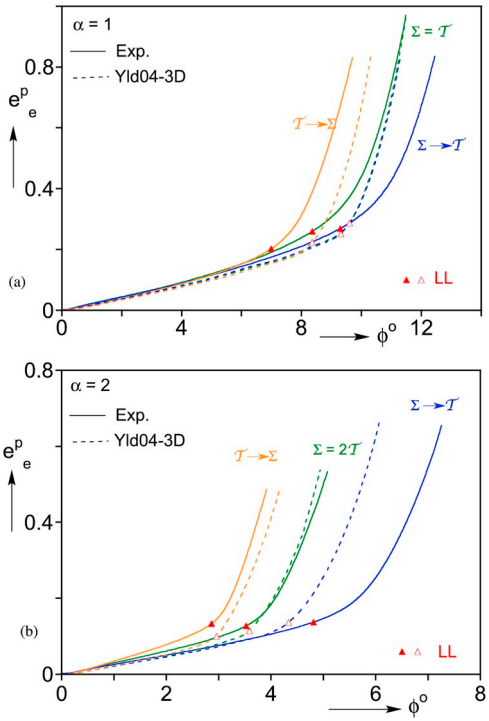

Fig. 17. Comparison of measured *Mean* equivalent plastic strain vs. rotation for the radial and corner paths and corresponding one calculated using Yld04-3D constitutive model.
(a) $\alpha = 1.0$ and (b) $\alpha = 2.0$.

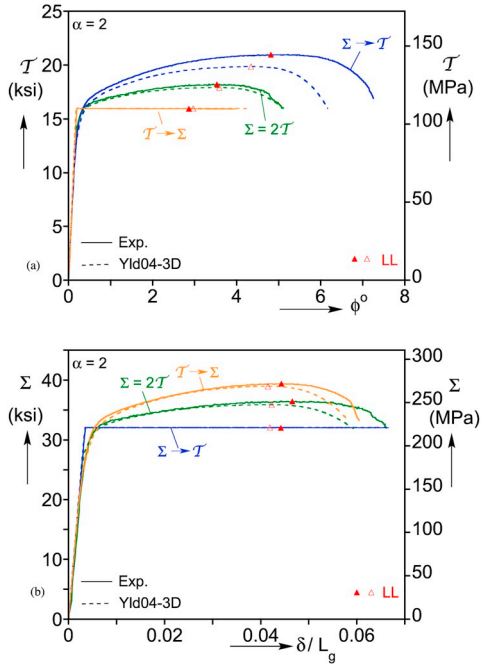

Fig. 18. Comparison of measured and calculated responses using Yld04-3D for the set of radial and corner path experiments with $\alpha = 2.0$. (a) Shear stress-rotation and (b) axial stress elongation.

Fig. 18 compares the calculated and measured stress responses for the three $\alpha = 2.0$ paths. The radial path predictions follow the measured responses very well for shear while for the axial stress the downturn occurs somewhat earlier. The equivalent strain trajectory in Fig. 17b matches the experimental one very well. Both of the $\boldsymbol{T} \rightarrow \Sigma$ stress responses are reproduced with similar level of agreement to the radial results and so is the equivalent strain-rotation trajectory in Fig. 17b. For the $\Sigma \rightarrow \boldsymbol{T}$ path the shear response traces a somewhat lower trajectory than the experimental one. The equivalent strain in Fig. 17b follows the trend of the measured results but the upswing occurs earlier. The predictions for the vM and H8 constitutive model were much worse and are not included here.

Overall the performance of the analysis in the corner paths is reasonably good but not as good as for the radial paths. The agreement with the measured results can be improved by including data from the corner paths in the calibration of the anisotropic yield function.

4. Summary and conclusions

Part II of this study presented an analytical framework for predicting the set of tension-torsion responses reported in Part I all of which exhibited limit load instabilities followed by extensive localized deformation that eventually resulted in failure. Motivated by the limited damage observed in Al-6061-T6 at high strains, the experiments are simulated using a customized constitutive model free of the "softening effects" of damage often used in failure predictions. The analysis incorporates a non-quadratic anisotropic yield function, a material hardening response extracted to large strains from a simple shear test, and appropriate finite element models.

The analysis successfully reproduced the measured biaxial stress-deformation responses starting from the onset of yielding; the stress levels in the extended branches that follows where the deformation in the test sections is homogeneous; the stress and deformation levels at which the load maxima occur; and the stress decaying branches associated with localized deformation. The analysis captured the geometry of the localization zones, the nearly exponential growth of strain in them and the associated sharp strain gradients to strain levels that correspond to the recorded failure strains. Most importantly, this level of success was achieved without the artificial introduction of any softening features to the constitutive model adopted (for alternate approaches to the modeling of tension-torsion experiments see for example Xue et al. (2013); Papasidero et al. (2014; 2015)). Following are observations, comments and conclusions derived from this analysis effort.

- An essential aspect of this successful performance of the analysis is first the adoption of a non-quadratic yield function suitable for Al-alloys, coupled to an accurate representation of the anisotropy induced to the tubes used in the experiments by the extrusion process. This was achieved using the Yld04-3D yield function with exponent 8, calibrated using the radial path biaxial stress states of the tension-torsion experiments of Part I together with the tension-pressure results presented in Appendix A,[I].
- A second essential component of such analyses that is often difficult to adhere to, is a stress-strain response that captures the hardening of the material to the strain levels reached in the experiments simulated. Because of the high strains recorded in the experiments, the material hardening was established from a pure torsion test on a tubular specimen. This test produced a stress-strain response to a much higher strain level than, for example, the value obtained from the necked zone of a tensile test using an inverse method. It was further demonstrated that the extraction of the material hardening must be accomplished using the constitutive model adopted in the simulation of the structural responses, which in this study meant the Yld04-3D yield function. In the simple shear test used the material frame rotates, which must be accounted for in the extraction of the material hardening when using an anisotropic yield function.
- The test specimen design allows the state of stress and strain in the test section to remain essentially uniform up to the attainment of the load maxima—the small amount of radial deflection in the test section can be neglected. Thus, the onset of the load maxima, important in structural design, can be evaluated from simple Considère-type considerations. The accuracy of such calculations is decisively dependent on the availability of an accurate representation of material hardening. This of course is equally applicable to the prediction of the load maxima by the numerical model.
- Localization is best modeled numerically using solid elements. Reproducing the high strain gradients that develop in the necked zones to the levels achieved in the experiments requires a very fine mesh in these zones.
- The aluminum alloy used in the experiments had very small initial porosity and very limited pore growth was observed outside the failure zone. Since the failure surfaces exhibited the dimpled relief associated with void growth, this must have occurred very close to the end of life of the material. This material characteristic is at least partly responsible for the successful reproduction of the local deformations to strain levels at which rupture occurred without the introduction of damage.
- The simulations reproduced the localized deformations that developed in the experiments at rupture. Termination of such analyses requires a failure criterion. A properly generated failure locus such as the one in Part I can be used to calibrate one of several existing expressions for failure strain vs. triaxiality and Lode parameters. Such expressions can then be used in large-scale calculations of structures under extreme loadings to terminate the life of material points and follow the progression of failure in the structure. For example, the exponential relationship of failure strain to triaxility of Johnson and Cook (1985) or the Hosford-Coulomb expression in Mohr and Marcadet (2015) lend themselves for such calculations.

Acknowledgments

The authors acknowledge with thanks financial support for this work received from the National Science Foundation through the

GOALI grant CMMI-1663269. Dr. Nicolas Tardif of INSA Lyon contributed significantly to the early efforts to simulate numerically such tension-torsion experiments for which we are grateful. We also thank Dr. Raja K. Mishra of General Motors for cooperation and technical interactions.

Appendix A. Calibration of Yld04-3D

The calibration follows broadly the procedure in Appendix B of Barlat et al. (2005) but using the tension-torsion, pressure-axial load, pure shear and uniaxial tension experiments presented in Part I (see also the calibrations in Tardif & Kyriakides (2012); Chen et al. (2016)). Through-thickness shear measurements are not available thus the anisotropy constants $\{c'_{44}, c'_{55}, c''_{44}, c''_{55}\}$ in Eq. (3) are assigned the value 1.0. The rest of the constants are determined by minimizing the error function that is developed below. The test sections in the experiments are assumed to be under plane stress represented by the vector:

$$\boldsymbol{\sigma} = (\sigma_{11}, \sigma_{22}, \sigma_{12})^T. \tag{A1}$$

(i) *Uniaxial Tension Test*

The plastic work is determined from the measured response as follows:

$$W^p = \int_0^{\varepsilon_{22}^w} \sigma_{22} d\varepsilon_{22}^p \tag{A2a}$$

where ε_{22}^w is the plastic strain at the chosen value of plastic work of 1000 psi (6.9 MPa) and σ_{22}^w is the corresponding stress. The uniaxial stress state is introduced in the current yield function (3) resulting in

$$\sigma_e = \Phi(\boldsymbol{\sigma}_u) \tag{A2b}$$

Using (A2) the following error function is established:

$$\mathcal{E}_u = \left(\frac{\sigma_e}{\sigma_{22u}^w} - 1 \right)^2 \tag{A3}$$

The R-value is determined by fitting linearly the measured $\varepsilon_{11}^p - \varepsilon_{22}^p$ data to obtain $r = -d\varepsilon_{11}^p / d\varepsilon_{22}^p$, and then

$$R_{uex} = \frac{d\varepsilon_{11}^p}{d\varepsilon_{33}^p} = \frac{r}{1-r} \tag{A4}$$

Use the flow rule to evaluate

$$d\varepsilon_{ij}^p = d\Lambda \frac{\partial \Phi}{\partial \sigma_{ij}} \tag{A5a}$$

at $\boldsymbol{\sigma} = (0, \sigma_{22}^w, 0)^T$ and establish the strain ratio predicted through (3),

$$R_{\Phi u} = d\varepsilon_{11}^p / d\varepsilon_{33}^p. \tag{A5b}$$

Then form the error function

$$\mathcal{E}_{Ru} = \left(\frac{R_{\Phi u}}{R_{exu}} - 1 \right)^2 \tag{A6}$$

(ii) *Pure Torsion Test*

Let ε_{12}^w be the shear strain corresponding to the chosen value of plastic work evaluated from

$$W^p = 2 \int_0^{\varepsilon_{12}^w} \sigma_{12} d\varepsilon_{12}^p = 1000 \text{ psi} \tag{A7a}$$

and σ_{12}^w be the corresponding stress. This pure shear stress-state is introduced into the current yield surface (3) resulting in

$$\sigma_e = \Phi(\boldsymbol{\sigma}_s) \tag{A7b}$$

The following error function is then established

$$\mathcal{E}_s = \left(\frac{\sigma_e}{\sigma_{22u}^w} - 1 \right)^2 \tag{A8}$$

(iii) *Pressure-Tension Tests*

For each of the seven $\sigma_{11} - \sigma_{22}$ radial paths performed, let $(\varepsilon_{11}^w, \varepsilon_{22}^w)$ be the strains corresponding to

$$W^p = \int_0^{\varepsilon_{11}^w} \sigma_{11} d\varepsilon_{11}^p + \int_0^{\varepsilon_{22}^w} \sigma_{22} d\varepsilon_{22}^p = 1000 \text{ psi}, \tag{A9a}$$

and $(\sigma_{11}^w, \sigma_{22}^w)$ be the corresponding stresses. This biaxial stress is introduced in the current yield surface (3) to produce

$$\sigma_e = \Phi(\boldsymbol{\sigma}_{PT}) \tag{A9b}$$

and the following error function is developed:

$$\mathcal{E}_{PT} = \left(\frac{\sigma_e}{\sigma_{22u}^w} - 1 \right)^2 \tag{A10}$$

The flow rule (A5a) is used to evaluate the strain increments for $(\sigma_{11}^w, \sigma_{22}^w, 0)^T$ and develop the predicted strain ratio $R_{\Phi PT} = d\varepsilon_{11}^p / d\varepsilon_{22}^p$. The following error function is then constructed:

$$\mathcal{E}_{RPT} = \left(\frac{R_{\Phi PT}}{R_{\text{exp}}} - 1 \right)^2 \tag{A11}$$

(iv) *Tension-Torsion Tests*

In these experiments the axial-to-shear stress ratio is prescribed to be:

$$\sigma_{22} = \alpha \sigma_{12} \tag{A12a}$$

while the hoop-to-axial ratio is

$$\sigma_{11} = \beta \sigma_{22} \tag{A12b}$$

The constant β is evaluated for each value of α as outline in Appendix B.

For each of the seven $\sigma_{22} - \sigma_{12}$ radial paths, let $(\varepsilon_{11}^w, \varepsilon_{22}^w, \varepsilon_{12}^w)$ be the strains corresponding to

$$W^p = \int_0^{\varepsilon_{11}^w} \sigma_{11} d\varepsilon_{11}^p + \int_0^{\varepsilon_{22}^w} \sigma_{22} d\varepsilon_{22}^p + 2\int_0^{\varepsilon_{12}^w} \sigma_{12} d\varepsilon_{12}^p = 1000 \text{ psi}, \tag{A13a}$$

and $(\sigma_{11}^w, \sigma_{22}^w, \sigma_{12}^w)$ the corresponding stresses. This state of stress is introduced in the current yield surface (3) to produce

$$\sigma_e = \Phi(\boldsymbol{\sigma}_{TT}) \tag{A13b}$$

which is then used to generate the following error function:

$$\mathcal{E}_{TT} = \left(\frac{\sigma_e}{\sigma_{22u}^w} - 1 \right)^2 \tag{A14}$$

The flow rule (A5a) is used to evaluate the strains for $(\sigma_{11}^w, \sigma_{22}^w, \sigma_{12}^w)^T$ and develop the strain ratios $R_{\Phi TT1} = d\varepsilon_{11}^p / d\varepsilon_{22}^p$ and $R_{\Phi TT2} = d\varepsilon_{12}^p / d\varepsilon_{22}^p$, which are used to form the following error function:

$$\mathcal{E}_{RTT} = \left(\frac{R_{\Phi TT1}}{R_{\text{exp1}}} - 1 \right)^2 + \left(\frac{R_{\Phi TT2}}{R_{\text{exp2}}} - 1 \right)^2 \tag{A15}$$

Finally, the optimal values of the anisotropy coefficients (c_{ij}', c_{ij}'') are then chosen by minimizing the following weighted sum of these error functions:

$$\mathcal{E}(c_{ij}', c_{ij}'') = \sum_m \omega_m \left(\frac{\sigma_{e\Phi}}{\sigma_{22u}^w} - 1 \right)_m^2 + \sum_n \omega_n \left(\frac{R_\Phi}{R_{ex}} - 1 \right)_n^2 \tag{A16}$$

In (A16) the first series represents the errors from the *m* flow stresses, the second the errors from the *n* strain ratios developed above. The variables (ω_m, ω_n) are weight functions that represent the confidence level assigned to each particular experiment. The minimization was performed using the routine *NMinimize* in Mathematica.

Appendix B. Estimation of β

In the tension-torsion radial path experiments, the test section develops a small amount of curvature that depends on the level of tension applied, or the ratio α. The hoop stress is assumed to be proportional to the axial stress through

$$\sigma_{11} = \beta \sigma_{22}. \tag{B1}$$

For values of $\alpha \leq 1.5$, the curvature developed in the axial direction is quite small. Thus β is estimated using Hosford's isotropic

yield function (1) in the flow rule to determine the following strain ratio:

$$R = \frac{d\varepsilon_{11}^{p}}{d\varepsilon_{22}^{p}} = \frac{\partial \Phi_{H8}}{\partial \sigma_{11}} / \frac{\partial \Phi_{H8}}{\partial \sigma_{22}} = f(\alpha, \beta). \tag{B2}$$

$f(\alpha, \beta)$ is assigned the hoop-axial strain ratio measured in the experiment in the crest of the axial curvature—at the stress levels associated with $W^p = 1000$ psi (6.9 MPa) Since α is known, β is evaluated from (B2) numerically.

For $\alpha > 1.5$, the axial curvature that develops is more significant. Let ρ_2 and ρ_1 be the measured radii of curvature in the axial and hoop direction respectively at the test section mid-height. We assume that this part of the test section is in membrane state of stress, which then satisfies the membrane equilibrium equation

$$\frac{\sigma_{11}}{\rho_1} - \frac{\sigma_{22}}{\rho_2} = 0. \tag{B3}$$

Eq. (B3) readily yields

$$\beta = \frac{\sigma_{11}}{\sigma_{22}} = \frac{\rho_1}{\rho_2}. \tag{B4}$$

The estimated values of β for the seven tension-torsion radial paths and the “plane-strain” experiments are listed in Table B1.

Table B1
Estimated values of the hoop-to-axial stress ratio, β for various values of α

α	0.5	0.75	1.0	1.5	2.0	3.0	4.0	∞
β	0.60	0.47	0.39	0.32	0.25	0.23	0.21	0.19

References

ABAQUS, 2016. Theory Guide. Section 1.4.3.
Barlat, F., Aretz, H., Yoon, J.W., Karabin, M.E., Brem, J.C., Dick, R.E., 2005. Linear transformation-based anisotropic yield functions. Int'l J. Plasticity 21, 1009–1039.
Chen, K., Scales, M., Kyriakides, S., Corona, E., 2016. Effects of anisotropy on material hardening and burst in the bulge test. Int'l J. Solids Struct. 82, 7–84.
Chen, K., Scales, M., Kyriakides, S., 2018a. Material hardening of a high ductility aluminum alloy from a bulge test. Int'l J. Mech. Sciences. 138–139, 476–488.
Chen, K., Scales, M., Kyriakides, S., 2018b. Effect of material frame rotation on the hardening of an anisotropic material in simple shear tests. ASME J. Applied Mech. 85 (124501), 1–5.
Dick, R.D., Yoon, J.W., 2018. Plastic anisotropy and failure in thin metal: material characterization and fracture prediction with an advanced constitutive model and polar EPS (effective plastic strain) fracture diagram for AA 3014-H19. Int'l J. Solids Struct. 151, 195–213.
Ghahremaninezhad, A., Ravi-Chandar, K., 2012. Ductile failure behavior of polycrystalline Al 6061-T6. Int'l J. Fracture 174, 177–202.
Ghahremaninezhad, A., Ravi-Chandar, K., 2013. Ductile behavior in polycrystalline aluminum alloy Al 6061-T6 under shear dominant loading. Int'l J. Fract. 180, 23–39.
Giagmouris, T., Kyriakides, S., Korkolis, Y.P., Lee, L.-H., 2010. On the localization and failure in aluminum shells due to crushing induced bending and tension. Int'l J. Solids Struct. 47, 2680–2692.
Gorji, M.B., Mohr, D., 2018. Predicting shear fracture of aluminum 6016-T4 during deep drawing: combining Yld-2000 plasticity with Hosford–Coulomb fracture model. Int'l J. Mech. Sci. 137, 105–120.
Ha, J., Baral, M., Korkolis, Y.P., 2018. Plastic anisotropy and ductile fracture of bake-hardened AA6013 aluminum sheet. Int'l J. Solids Struct. 155, 123–139.
Haltom, S.S., Kyriakides, S., Ravi-Chandar, K., 2013. Ductile failure under combined shear and tension. Int'l J. Solids Struct. 50, 1507–1522 2013.
Hill, R., 1950. The Mathematical Theory of Plasticity. Clarendon Press, Oxford.
Hosford, W.F., 1972. A generalized isotropic yield criterion. ASME J. Applied Mechanics 39, 607–609.
Johnson, G.R., Cook, W.H., 1985. Fracture characteristics of three metals subjected to various strains, strain rates, temperatures and pressures. Eng. Fract. Mech. 21, 31–48.
Kang, J., Wilkinson, D.S., Wu, P.D., Bruhis, M., Jain, M., Embury, J.D., Mishra, R.K., 2008. Constitutive behavior of AA5754 sheet materials at large strains. J. Eng. Mater. Technol. 130, 1–5 031004.
Korkolis, Y.P., Kyriakides, S., 2008. Inflation and burst of aluminum tubes part II: an advanced yield function including deformation-induced anisotropy. Int'l J. Plasticity 24, 1625–1637.
Korkolis, Y.P., Kyriakides, S., 2009. Path dependent failure of inflated aluminum tubes. Int. J. Plast. 25, 2059–2080.
Korkolis, Y.P., Kyriakides, S., Giagmouris, T., Lee, L.-H., 2010. Constitutive modeling and rupture predictions of Al-6061-T6 tubes under biaxial loading paths. ASME J. Applied Mechanics 77 (5), 1–5 064501.
Lee, J.-Y., Lee, K.J., Kuwabara, T., Barlat, F., 2018. Numerical modeling for accurate prediction of strain localization in hole expansion of a steel sheet. Int'l J. Solids Struct. 156–157, 107–118.
Logan, R.W., Hosford, W.F., 1980. Upper-bound anisotropic yield locus calculations assuming < 111 > -pencil glide. Int'l J. Mech. Sci. 22, 419–430.
Mohr, D., Marcadet, S.J., 2015. Micromechanically-motivated phenomenological Hosford–Coulomb model for predicting ductile fracture initiation at low stress triaxialities. Int'l J. Solids Struct. 67, 40–55.
Papasidero, J., Doquet, V., Mohr, D., 2014. Determination of the effect of stress state on the onset of ductile fracture through tension-torsion experiments. Exp. Mech. 54, 137–151.
Papasidero, J., Doquet, V., Mohr, D., 2015. Ductile fracture of aluminum 2014-T351 under proportional and non-proportional multi-axial loading: bao-Wierzbicki results revisited. Int'l J. Solids Struct. 69–70, 459–474.
Scales, M., Tardif, N., Kyriakides, S., 2016. Ductile failure of aluminum alloy tubes under combined torsion and tension. Int'l J. Solids Struct. 97–98, 116–128.
Tardif, N., Kyriakides, S., 2012. Determination of anisotropy and material hardening for aluminum sheet metal. Int'l J. Solids Struct. 49, 3496–3506.
Tian, H., Brownell, B., Baral, M., Korkolis, Y.P., 2017. Earing in cup-drawing of anisotropic Al-6022-T4 sheets. Int'l J. Mater. Forming 10, 329–343.
Xue, Z., Faleskog, J., Hutchinson, J.W., 2013. Tension-torsion fracture experiments-Part II: simulation with the extended Gurson model and a ductile fracture criterion based on plastic strain. Int'l J. Solids Struct. 50, 4258–4269.
Yoon, J.W., Barlat, F., Dick, R.E., Karabin, M.E., 2006. Prediction of six or eight ears in a drawn cup based on a new anisotropic yield function. Int'l J. Plasticity 22, 174–193.
Yoon, J.W., 2009, 2011. Personal Communications. 2009. .